*remote sensing*

MDPI

*Article*

# A Study on Typhoon Center Localization Based on an Improved Spatio-Temporally Consistent Scale-Invariant Feature Transform and Brightness Temperature Perturbations

**Chaoyu Yan [1,2], Jie Guang [1,*], Zhengqiang Li [1,3], Gerrit de Leeuw [1,4] and Zhenting Chen [5]**

[1] State Environmental Protection Key Laboratory of Satellite Remote Sensing & Key Laboratory of Remote Sensing and Digital Earth, Aerospace Information Research Institute, Chinese Academy of Sciences, Beijing 100101, China; yanchaoyu23@mails.ucas.ac.cn (C.Y.); lizq@radi.ac.cn (Z.L.); g.d.leeuw@hotmail.com (G.d.L.)
[2] University of Chinese Academy of Sciences, Beijing 100049, China
[3] School of Remote Sensing Science and Technology, Aerospace Information Technology University, Jinan 250200, China
[4] Royal Netherlands Meteorological Institute (KNMI), R&D Satellite Observations, 3731GA De Bilt, The Netherlands
[5] School of Information Engineering, Kunming University, Kunming 650214, China; cztgis@163.com
* Correspondence: guangjie@aircas.ac.cn

**Abstract:** Extreme weather events like typhoons have become more frequent due to global climate change. Current typhoon monitoring methods include manual monitoring, mathematical morphological methods, and artificial intelligence. Manual monitoring is accurate but labor-intensive, while AI offers convenience but requires accuracy improvements. Mathematical morphology methods, such as brightness temperature perturbation (BTP) and a spatio-temporally consistent (STC) Scale-Invariant Feature Transform (SIFT), remain mainstream for typhoon positioning. This paper enhances BTP and STC SIFT methods for application to Fengyun 4A (FY-4A) Advanced Geosynchronous Radiation Imager (AGRI) L1 data, incorporating parallax correction for more accurate surface longitude and latitude positioning. The applicability of these methods for different typhoon intensities and monitoring time resolutions is analyzed. Automated monitoring with one-hour observation intervals in the northwest Pacific region demonstrates high positioning accuracy, reaching 25 km or better when compared to best path data from the China Meteorological Administration (CMA). For 1 h remote sensing observations, BTP is more accurate for typhoons at or above typhoon intensity, while STC SIFT is more accurate for weaker typhoons. In the current era of a high temporal resolution of typhoon monitoring using geostationary satellites, the method presented in this paper can serve the national meteorological industry for typhoon monitoring, which is beneficial to national pre-disaster prevention work as well as global meteorological research.

**Keywords:** typhoon; location; SIFT; brightness temperature perturbations

check for updates

**Citation:** Yan, C.; Guang, J.; Li, Z.; de Leeuw, G.; Chen, Z. A Study on Typhoon Center Localization Based on an Improved Spatio-Temporally Consistent Scale-Invariant Feature Transform and Brightness Temperature Perturbations. *Remote Sens.* **2024**, *16*, 4070. https://doi.org/10.3390/rs16214070

Received: 19 September 2024
Revised: 19 October 2024
Accepted: 23 October 2024
Published: 31 October 2024

**Copyright:** © 2024 by the authors. Licensee MDPI, Basel, Switzerland. This article is an open access article distributed under the terms and conditions of the Creative Commons Attribution (CC BY) license (https://creativecommons.org/licenses/by/4.0/).

## 1. Introduction

In recent years, global environmental change has accelerated, extreme weather events have generally increased, and typhoon activity has become more frequent [1]. Typhoons are destructive weather events that bring strong winds, heavy rain, and storm surges. They often cause significant economic losses and threaten the safety of lives in coastal areas. To mitigate adverse effects of typhoons, it is extremely important to locate typhoons in real time.

Typhoon formation relies mainly on the following conditions: sea surface water temperature above 26.5 °C; small shear of the ambient wind in the vertical direction; some initial disturbance of positive vorticity; and low pressure or cloud disturbance at least a few latitudes from the equator [2]. In view of these conditions for typhoon formation, the

tropical northwest Pacific is a typhoon-prone area. Following the statistics of the China Meteorological Administration (CMA) in the past decade, more than 20 typhoons form each year in the northwest Pacific Ocean. Tropical cyclones are classified into the following six categories (https://tcdata.typhoon.org.cn/data/doc/TC_std.pdf, accessed on 9 May 2006): a Tropical Depression (TD), Tropical Storm (TS), Severe Tropical Storm (STS), Typhoon (TY), Severe Typhoon (ST), and Super Typhoon (STY).

Typhoon monitoring refers to the use of various vehicles to record various physical phenomena, processes, and changes in meteorological elements within the typhoon, and its monitoring means mainly include aircraft monitoring, ground-based monitoring, radar monitoring, and satellite monitoring [3]. Currently, a crucial method for typhoon monitoring involves the utilization of meteorological satellites. Meteorological satellites have become indispensable sources of meteorological data globally, providing essential information for scientific research and everyday applications. They also play a critical role in typhoon monitoring [4]. The detection of typhoon position based on satellite remote sensing can help to quickly determine the generation of typhoons and their location, which is helpful for governments to take adequate preventive measures before the arrival of disasters, and can also help researchers to carry out research in the direction of global climate change.

Current methods of typhoon identification and localization using satellite imagery are mainly classified into manual monitoring, mathematical morphological methods, and artificial intelligence methods. The initial typhoon positioning and some practical operations in China and abroad use the manual positioning method, which mainly relies on the experience of the staff and some characteristics of the typhoon. The results from the manual method are subjective and the positioning results vary greatly from staff to staff. Currently, most tropical cyclone warning centers in the world utilize the Dvorak method [5–7] for typhoon localization.

The initial studies on the mathematical morphology method of typhoon localization mainly used radar data [8–10]. Liu, et al. [11] introduced a method for detecting the center of typhoons through the intersection of the Zero Radial Velocity Line (ZRVL) obtained from a dual-Doppler radar system. This method is applicable to regions where data from Automatic Weather Stations (AWSs) are unavailable. Typhoon localization based on radar data has higher localization accuracy in the case of better radar echo quality as well as typhoon structure, but not in the case of weaker typhoon intensity.

By employing the spiral analysis method, which involves extracting spiral lines from satellite cloud imagery that reflect cloud features, and subsequently employing an algorithm for fitting, the polar coordinate origin of the spiral line is determined as the center of the typhoon [12–14]. When using a spiral analysis to locate typhoons, the results depend on the characteristics of the typhoon itself, and the thresholds set by the algorithm are not suitable for most cases and need to be adjusted for each situation.

Typhoon center localization is also possible using the method of a wind field analysis [15–17]. Zhang, et al. [18] proposed a multi-channel satellite cloud image fusion method based on a shear wave transform, and the results showed that the fused images obtained by the proposed algorithm improved the typhoon center localization accuracy and outperformed the comprehensive performance of similar image fusion algorithms. Liu and Wang [19] used infrared sequence images from the FY-2 meteorological satellite to perform pyramidal decomposition and construct a cloud-guided wind field based on a weighted median filtered optical flow model as a way to calculate the typhoon center using a density matrix. The wind field analysis method is applicable to the weaker incipient and extinction periods of typhoons. When the typhoon intensity is high, the wind field environment inside the typhoon is complex, and the accuracy of using the wind field to locate the typhoon center position will be greatly reduced.

In several studies, typhoon edge contour features or image grayscale thresholds have been used to automatically extract typhoon cloud systems and locate their centers [20–22]. Jaiswal and Kishtawal [23] extracted thermal cyclone center spiral features from geostation-

ary infrared satellite (Meteosat-5) image data to fit the location of the typhoon center by setting certain threshold values for typhoon center localization. These authors calculated the flux convergence point of the brightness temperature (BT) gradient vector and averaged the accumulated fractional values in the density matrix, and the typhoon center location was the highest scoring location. Zhang, et al. [24] proposed an efficient algorithm for typhoon center localization using fractal features and gradients of infrared satellite cloud images. Liu, Wang, Liao, and Fang [3] proposed a typhoon localization algorithm based on the spatio-temporally consistent (STC) Scale-Invariant Feature Transform (SIFT) method to filter the feature points after typhoon matching, and on this basis, the localization of the current typhoon center coordinates was completed. Xie, et al. [25] analyzed the spatial distribution characteristics of brightness temperature perturbation (BTP) in the center regions of typhoons during different time periods. They introduced a typhoon localization method based on brightness temperature data from FY-4A AGRI, known as the Bright-Temperature Perturbation (BTP) typhoon localization method. This algorithm effectively captures the brightness temperature perturbation features at the typhoon center, resulting in high accuracy in typhoon center localization. The BTP typhoon localization method is based on the brightness temperature perturbation factor, which effectively characterizes the state of typhoons during different time periods and in various spatial contexts. It demonstrates distinct advantages in localizing strong typhoons. On the other hand, the STC SIFT typhoon localization algorithm relies on the distribution of characteristic points in two successive images and the relative position of the typhoon center to these points. The STC SIFT method provides good localization accuracy, particularly when dealing with typhoons of weaker intensity. In summary, the BTP and the STC SIFT typhoon localization algorithms are the more commonly used and more accurate algorithms in the mathematical morphological method of typhoon localization.

In recent years, emerging artificial intelligence technologies have also been applied to typhoon identification and location. Permyakov, et al. [26] proposed methods for the estimation of typhoon eyewall characteristics (the center location, the radius and the width, and radii of inner and outer boundaries) based on World Wide Lightning Location Network (WWLLN) data. Magee, et al. [27] used multivariate Poisson regression and considering up to five modes of ocean-atmospheric variability and teleconnection patterns that influence TC behavior, thousands of possible predictor model combinations were compared using an automated variable selection procedure. Kang and Park [28] studied the precipitable water vapor (PWV) variation in a typhoon in 2018 based on the Global Navigation Satellite System (GNSS) inversion of PWV to predict the typhoon path. Some scholars [29,30] carried out work on a typhoon vortex identification model based on deep image target detection, an intelligent typhoon intensity determination model based on image classification and retrieval, and a typhoon fast and enhanced identification model, and constructed a typhoon intelligent monitoring and forecasting system. Although artificial intelligence technology can be more convenient to achieve fully automated typhoon identification and positioning, the accuracy of the current positioning still needs to be improved.

The mainstream typhoon center localization method is the mathematical morphology method, with the typhoon localization algorithm based on the STC SIFT [3] and the BTP algorithm [25], which are most effective in locating the typhoon center. In this paper, the BTP and STC SIFT typhoon localization methods are improved and applied to Fengyun 4A (FY-4A) Advanced Geosynchronous Radiation Imager (AGRI) data to automatically perform typhoon localization in the northwest Pacific region. FY-4A AGRI L1 data and the FY-4A AGRI cloud top height (CTH) product are used for projection conversion and cloud system identification. Parallax correction is added to make the longitude and latitude of typhoon positioning closer to the surface longitude and latitude. The research area and data used are described in Section 2 and the methodology is explained in Section 3. The use of the improved methods is demonstrated in Section 4 by application to FY-4A AGRI level 1 data collected over the study area on 6 November 2019, at 02:00 Beijing time, for Typhoon Halong (HL) 1923. In Section 5, the two algorithms are applied to the full time series

of six other typhoons with different intensities, observed with different time samplings (1–6 h). The results are analyzed based on comparison with optimal path data for the same typhoons provided by CMA. Section 6 quantifies the errors in typhoon localization using the two methods and provides a more in-depth analysis and discussion. Conclusions are presented in Section 7.

## 2. Data and Methods

### *2.1. Research Area*

The study reported in this paper was conducted over the northwest Pacific Ocean in the area 100°E–170°E, 5°N–45°N (Figure 1). The northwest Pacific warm pool serves as a significant genesis area for typhoons worldwide, with tropical cyclones forming throughout the year. On average, about 35 tropical cyclones develop annually in this region, and approximately 80% of them eventually develop into typhoons. Furthermore, roughly a quarter of these typhoons annually impact the coastal areas of China. Approximately 70% of the annual typhoon activity is concentrated in the months July to October, with August and September being the peak period for typhoon formation.

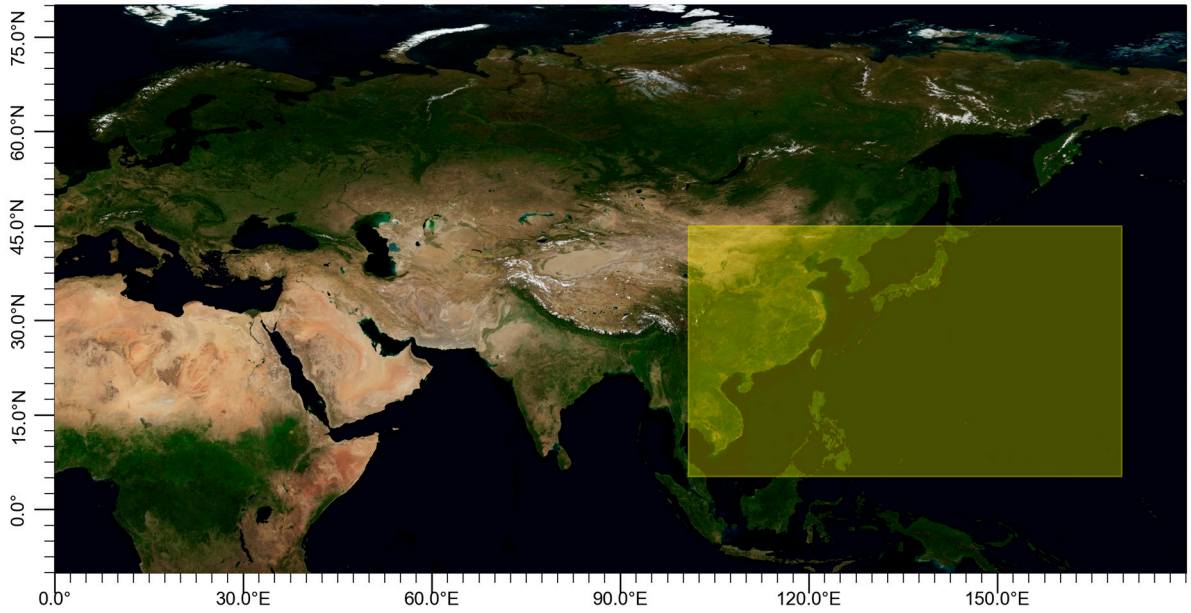



**Figure 1.** The yellow rectangular box represents the study area.

### *2.2. Research Data*

#### 2.2.1. FY-4A Advanced Geostationary Orbit Radiation Imager (AGRI) Data

Fengyun-4A (FY-4A) is the first of a series of seven second-generation Geostationary Earth Orbit (GEO) quantitative remote sensing meteorological satellites owned and operated by CMA (https://www.eoportal.org/satellite-missions/fy-4, last access: 23 March 2024), replacing Fengyun-2. FY-4A was launched on 11th December 2016. FY-4A carries the Advanced Geosynchronous Radiation Imager (AGRI), which covers a wavelength range from 0.45 to 13.8 μm with a spatial resolution of 4 km. Level 1 (L1) full-disk data are observed every hour, the observation time is 15 min past the whole hour, and two encrypted observations are made every 3 h from 0:00 to 21:00 (UTC), so 40 full-disk observations can be obtained every day [31]. FY-4A AGRI data are stored in HDF5 format, including grayscale data in 14 channels, calibration data for each band, observation time and start/stop position of each line, etc. FY-4A data have been publicly accessible since the summer of 2018 from the Fengyun Satellite Data Center (https://satellite.nsmc.org.cn/portalsite/default.aspx, last access: 23 March 2024) of the National Satellite Meteorological Center (NSMC) in China. In this paper, channel 12 thermal infrared data (wavelength: 10.3–11.3 μm) from the FY-4A

AGRI sensor are selected to derive the cloud brightness temperature (BT) as described in Section 3.2.

#### 2.2.2. Cloud Top Height Data (CTH)

The cloud top height product (CTH) retrieved from AGRI L1 data provides the cloud top height for each AGRI pixel. This product is retrieved from observations in the $CO_2$ absorption channel (13.3 μm) and two infrared channels (11.2 μm and 12.4 μm). A radiative transfer model and a one-dimensional variational method are used to obtain the cloud top temperature (CTT), from which cloud top height is calculated by combining information on the atmospheric temperature field from a numerical weather prediction model [32]. The CTH product is an important parameter for making parallax corrections to FY-4A AGRI data (Section 3.3).

#### 2.2.3. Optimal Path Data

The optimal path dataset used in this paper was obtained from CMA (https://tcdata.typhoon.org.cn, last access: 28 March 2024) [33,34]. This website is a real-time typhoon path release system that can accurately provide the latest and most comprehensive real-time typhoon information, including information on the center location, central pressure, maximum wind speed, moving direction, and forecasted path, as well as integrated precipitation forecasts. The system also integrates precipitation forecasts, satellite cloud maps, and weather conditions. In this paper, we mainly use the optimal path data provided by CMA for comparison with the results obtained from the methods developed as described below.

Seven typhoons were selected for the current study: Typhoon Halong (HL) 1923 in the year 2019; Typhoon Conson (CS) 2113 and Typhoon Kompasu (KPS) 2118 in the year 2021; Typhoon Malakas (MLK) 2201, Typhoon Songda (SD) 2205, and Typhoon Hinnamnor (HNM) 2211 in the year 2022; and Typhoon Haikui (HK) 2311 in the year 2023. The characteristics of these 7 typhoons and the time sampling with which they were observed during different stages of development are presented in Tables 1 and 2. The time sampling of CS and KPS is long with time samplings of 6 h, the time sampling of MLK is mostly 3 h, and the time sampling of HL, SD, HNM, and HK is short with most time sampling being 1 h.

**Table 1.** Characteristics of the seven typhoons selected for the study.

| Typhoon Name | Time | Amount of Data | Observation Time Resolution (h) | Typhoon Intensity | Average Wind Speed (m/s) | Average Travel Speed (km/h) |
|---|---|---|---|---|---|---|
| HL | 2019.11.01~2019.11.10 | 199 | 1 | TD~STY | 35.3 | 19.4 |
| CS | 2021.09.05~2021.09.13 | 34 | 6 | TD~STS | 22.29 | 12.4 |
| KPS | 2021.10.08~2021.10.14 | 27 | 6 | TD~TY | 22.42 | 15.48 |
| MLK | 2022.04.08~2022.04.14 | 68 | 3 | TS~ST | 27.8 | 32.23 |
| SD | 2022.07.28~2022.08.02 | 115 | 1 | TD~TS | 16.4 | 22.89 |
| HNM | 2022.08.28~2022.09.06 | 203 | 1 | TS~STY | 40.88 | 28.01 |
| HK | 2023.08.28~2022.09.06 | 187 | 1 | TD~STY | 28.36 | 17.07 |

**Table 2.** Amount of data observed at different stages of seven selected typhoons.

| Typhoon Name | TD | TS | STS | TY | ST | STY |
|---|---|---|---|---|---|---|
| HL | 60 | 18 | 12 | 35 | 26 | 48 |
| CS | 10 | 4 | 20 | | | |
| KPS | 6 | 13 | 7 | 1 | | |
| MLK | 7 | 17 | 19 | 11 | 10 | 4 |
| SD | 45 | 70 | | | | |
| HNM | | 27 | 18 | 36 | 41 | 81 |
| HK | 27 | 24 | 82 | 37 | 11 | 6 |

## 3. Methodology

Figure 2 shows the flow chart for the typhoon automatic center positioning process described in this study, with the following main steps:

1. AGRI L1-level product projection conversion pre-processing;
2. Cloud system identification in the study area images;
3. The parallax correction of the longitude and latitude of the target cloud system;
4. Typhoon localization algorithm based on space–time consistent SIFT;
5. Brightness temperature perturbation typhoon localization algorithm.

Each step is discussed below (Sections 3.1–3.5) and illustrated in Figures 3–7 of Section 4 where the typhoon automatic center positioning algorithm is applied. In brief, steps 1–3 are the preparation of the images for the identification and localization of the cloud system in geographic coordinates with reference to the Earth system. Steps 4 and 5 are the two actual typhoon center positioning methods by the application of different techniques to cropped images where only the typhoon cloud system is considered to determine the typhoon center location and the displacement is calculated from two consecutive images, referred to as the current and the previous images.

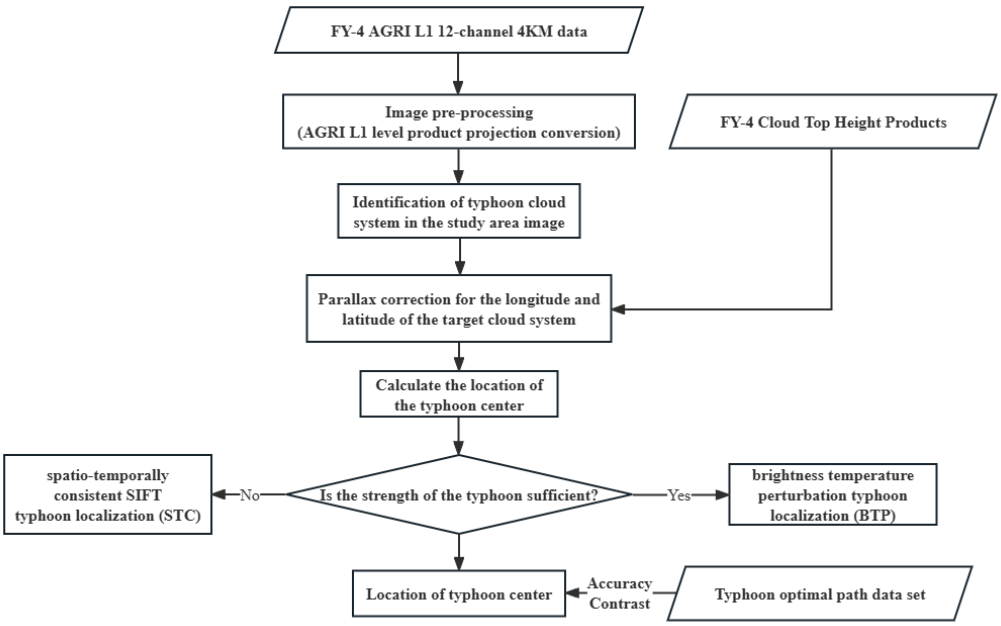



**Figure 2.** Typhoon automatic center positioning process.

### *3.1. AGRI L1-Level Product Projection Conversion Pre-Processing*

Because the study described in this paper uses typhoon positioning in longitude and latitude coordinates, the row and column numbers of the image are converted to the corresponding longitude and latitude. The FY-4A satellite position is computed using the nominal projection of the geostationary orbit defined by the CGMS LRIT/HRIT global specification. The geographic coordinates are calculated with reference to the WGS84 reference ellipsoid [25]. Using this method, we obtained the entire image corresponding to the study area.

### *3.2. Image Cloud System Identification*

In this study, the cloud system characteristics are derived from the patterns of the cloud brightness temperature (BT) available from AGRI observations at wavelengths in the thermal infrared part of the spectrum, in channel 12 (Section 2.2.1). To convert the measured radiances to BT, the channel 12 images of the AGRI L1 full-disk data are first cropped using the longitude and latitude of the study area. Then, the original AGRI channel 12 data are

converted to BT data using the channel 12 calibration data, and the BT data are assigned to different classes using the Fisher criteria [35] for small and large intra-class variances to automatically find the thresholds. Typhoon cloud systems generally cover a large area, and using erosion and expansion, some smaller cloud systems and clouds can be removed to reduce interference. After further removing cloud systems with an area of less than 1500 pixels, the target cloud system is localized by searching for the cloud system with the nearest center of mass coordinates to the last localized typhoon center. The target cloud system image is cropped, but its longitude and latitude correspond to those of the cloud top. Therefore, the method described in Section 3.3 is required to correct the longitude and latitude from the cloud top to the surface.

### *3.3. Parallax Correction for the Longitude and Latitude of the Target Cloud System*

The satellite observation method and the curvature of the Earth lead to a field-of-view bias resulting in the deviation in the longitude and latitude of the clouds obtained from the satellite observation from the corresponding longitude and latitude of the sub-satellite ground surface. The actual longitude and latitude of the cloud were calculated following the method described by Di et al. [32], who used the CTH data to correct the parallax of the projected transformed image, as described below.

In Figure 3, S is the location of the satellite, A is the coordinate of the corresponding sub-satellite point ($\lambda_S$, 0), O is the center of mass of the Earth, T is the actual position of the cloud, X is the position of the cloud projected on the surface (the cloud height is h), and P is the position of the cloud observed by the satellite ($\lambda_P$, $\psi_P$). Let the radius of the Earth be r, the height of the geostationary satellite from the surface be H, the geocentric distance R = H + r, the distance from the satellite S to the position P of the observed cloud be L, and the parallax angle ∠POX = α. Also, let ∠OSP = β and ∠POA = γ.

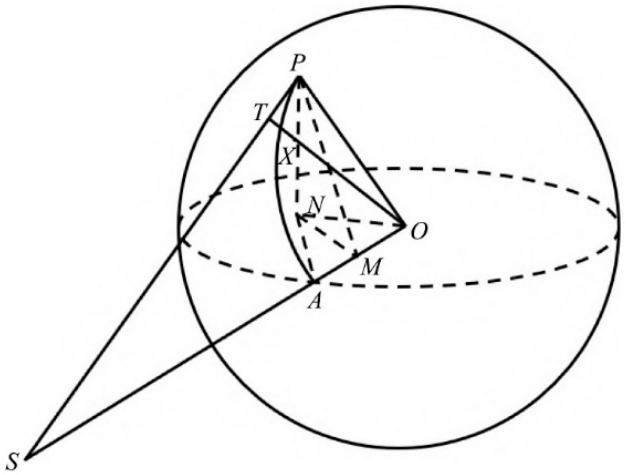



**Figure 3.** Parallax correction geometry relationship model [32].

First, calculate γ:

$$\gamma = \arccos(\cos(\psi_P) \times \cos(\lambda_S - \lambda_P)) \quad (1)$$

Then, calculate the parallax angle α:

$$\alpha = \arcsin\left(\frac{R \times \sin(\gamma)}{L}\right) - \arcsin\left(\frac{R \times r \times \sin(\gamma)}{L \times (h + r)}\right) \quad (2)$$

$$\text{where } L = \sqrt{r^2 + R^2 - 2 \times r \times R \times \cos(\gamma)} \quad (3)$$

Finally, the actual latitude of the cloud can be obtained as

$$\psi_X = \arcsin\left(\frac{sin(\psi_P) \times sin(\gamma - \alpha)}{sin(\gamma)}\right) \tag{4}$$

The actual longitude of the cloud is obtained as

$$\lambda_X = \lambda_S \pm \arccos\left(\frac{\cos(\gamma - \alpha)}{\cos(\psi_X)}\right) \tag{5}$$

In the above equation, the negative sign is taken when the observed longitude of the cloud is less than that of the sub-satellite point, and the positive sign is taken when the opposite is true.

This method was demonstrated to be effective in correcting the longitude and latitude of the observed cloud top to the corresponding actual longitude and latitude with reference to the sub-satellite Earth surface, in the experiments of Di et al. [32].

### *3.4. Spatio-Temporally Consistent (STC) SIFT Typhoon Localization Algorithm*

The STC SIFT typhoon localization algorithm primarily relies on the relationship between characteristic points in the current typhoon image and those in the previous typhoon image. This relationship is used to determine the current typhoon's center coordinates and is applied to the cropped image, which only retains the typhoon cloud system rather than the whole study area. The SIFT feature extraction algorithm was first proposed by Lowe [36] and was improved by some scholars [3,37,38]. In the current study, the typhoon localization algorithm based on STC SIFT [3] is used as the starting point for further improvement. The algorithm by Liu, Wang, Liao, and Fang [3] uses the longitude and latitude coordinates of the previous typhoon center along with its corresponding satellite image as historical information for localization. Firstly, based on the longitude and latitude information of the previous typhoon center, they extracted the corresponding image from the current satellite image. The size of the image is related to the time sampling between the previous and current time sampling. The longer the interval, the larger the potential range of typhoon movement, and thus the larger the area set. Then, they matched the typhoon cloud system in this area with the typhoon cloud system in the previous image to determine the current typhoon center position. In the algorithm improved in this study, we extract the corresponding image from the current satellite data using the longitude and latitude of the center of the target cloud system obtained in Section 3.2. The size of the two consecutive images is the same. The algorithm primarily consists of four steps: feature point extraction, spatio-temporal consistency feature selection, regular angular distribution feature selection, and typhoon center localization.

The speed of typhoon movement varies, with an average speed ranging from 20 to 30 km per hour. Additionally, the typhoon center does not move along a straight line at a constant speed. Sometimes, new centers may form near the original center, replacing it, resulting in potentially faster movement within a short period. Therefore, we set the upper limit for the variation in the typhoon center position to 60 km/h. The characteristic points around the typhoon not only undergo translational motion with the typhoon center but also exhibit their own rotational motion. The angular velocity of this rotation varies depending on the distance from the typhoon center; points closer to the center rotate at a higher angular velocity. To describe the range of speed variation in these characteristic points, a small increment is added to the typhoon's movement speed. The maximum selected variation in the speed of characteristic points is 80 km/h.

Spatio-temporal consistency feature selection is mainly based on the time sampling between the two images and the calculation of the displacement of corresponding feature points during that time. The maximum rate of change between the calculated feature points is 80 km/h, and the spatial resolution of the image is 4 km, so the maximum displacement

of the typhoon cloud system feature point movement radius $R_f$ during the time sampling T between the two images is given by

$$R_f = 20 \text{ Pixel/Hour} \times T, \tag{6}$$

The matching results of feature points may be unevenly distributed in space. The application of regular angular distribution feature selection can alleviate such situations. Rotationally uniform distribution filtering takes the center of previous positioning as the coordinate origin, divides the 360 degrees around a circle into 36 equal parts of 10 degrees each, and keeps only 1 feature point with the best match in each of these 36 sectors.

The current and previous images are pre-processed separately, including cloud system identification, parallax correction, and cropping the target cloud system. The current and previous images are centered at the geometric centers of the target cloud system in each of the respective images and both images are cropped to 320 × 320 pixels. The feature points in the two images are extracted and matched using the SIFT algorithm. The matched feature points are filtered using the STC and rotation uniform distribution filtering algorithms. The upper limit of the variation range of the typhoon center position is 60 km/h by default, so the maximum typhoon center movement $R_c$ during the time T between the observation of the two images is

$$R_c = 15 \text{ Pixel/Hour} \times T \tag{7}$$

The typhoon center location in the current image is determined as the point for which the proximity to the feature points is closest to the proximity of the typhoon center in the previous image to the corresponding feature points. This point is determined by minimizing the distance and angle deviations given by

$$\alpha = \arg\min_{\alpha \in \Omega} \sum_{i=1}^{N} \left| \|x_i - \alpha\|_F - \|x_i^* - \beta\|_F \right| \tag{8}$$

The minimum angular deviation is calculated using

$$\alpha = \arg\min_{\alpha \in \Omega} \sum_{i=1}^{N} \left\langle \frac{x_i - \alpha}{\|x_i - \alpha\|_F}, \frac{x_i^* - \beta}{\|x_i^* - \beta\|_F} \right\rangle, \tag{9}$$

where $x_i$ is the feature point in the current typhoon cloud map, $x_i^*$ is the matching feature point of $x_i$ in the previous typhoon cloud map, $\alpha$ is the center position of the current typhoon, $\beta$ is the center position of the previous typhoon, $N$ is the number of all matching feature points, $\|A\|_F = \left(\sum_{ij} {a_{ij}}^2\right)^{\frac{1}{2}}$, $\Omega = (\|\alpha - \beta\|_F < R_c)$, and $R_c$ is the radius of typhoon center movement. Formulas (8) and (9) search for point a within the radius R centered at b that satisfies the two equations mentioned above. After finding the locations of the minimum distance and angle deviations, the gradients of the two methods with respect to the surrounding points are calculated. The solution with the largest gradient is selected as the final result and the current image typhoon center is the location where the deviation is minimal.

### *3.5. Brightness Temperature Perturbation (BTP) Typhoon Location Method*

The brightness temperature perturbation (BTP) typhoon location method is inspired by the wind stress perturbation theory. Chelton, et al. [39] used the QuikSCAT satellite radar scatterometer to measure near-surface wind speed and direction over the global ocean at a 25 km resolution, showing that cyclone scattering and spin have persistent small-scale features in the dynamics and thermodynamics of wind stress. Maloney and Chelton [40] analyzed observations of wind stress from the NASA sea wind scatterometer and the advanced microwave scanning radiometer and found that wind stress increased linearly with increasing sea surface temperature. Minobe, et al. [41] studied the effect of sea surface temperature fronts on precipitation using an atmospheric model and noted

that typhoon clouds form with very low cloud top temperatures. The study by Wei, et al. [42] showed that there is a significant positive correlation between the wind stress dispersion and rotation and the perturbation of sea surface temperature. Correspondingly, the wind field disturbances caused by mesoscale sea surface temperature perturbations over the ocean can also lead to changes in the marine environment. Changes in the wind field can result in alterations in surface momentum and heat flux, thereby impacting the oceanic environment.

Brightness temperature perturbation (BTP) refers to the variation or deviation in brightness temperature (BT) from its average value or baseline state at a specific observation point or region. BTP is commonly used to analyze dynamic processes in the atmosphere or ocean, such as the impact of weather systems and ocean temperature changes on climate and meteorological conditions. The BTP typhoon location method used in the current study is an improvement in the BTP typhoon localization method of Xie et al. [25]. Xie et al. [25] used a polynomial interpolation method for short-term typhoon forecast data provided by the Typhoon and Ocean Meteorological Forecast Center of CMA as an initial guess for the location of the current typhoon center. BT gradients within a window around the estimated location were used to provide the actual typhoon center location. In the current study, the BTP typhoon localization method primarily utilizes the typhoon's BT images to calculate perturbation values in the central region, rather than the entire typhoon. This is because the algorithm uses the geometric center of the cloud system as the center, with a radius of 40 km and a step size of 8 km as the search range, to search for the maximum BTP value within the typhoon center. The algorithm centers the image at the geometric center of the target cloud system to intercept the image of the corresponding size based on the time sampling between the current and previous images. A higher time sampling results in smaller cropped image sizes. Parallax correction is added to correct the longitude and latitude determined by the typhoon positioning to obtain the surface-referenced longitude and latitude of the cloud system and the images are cropped to retain only the target cloud system.

For the application of the BTP typhoon localization method, the original AGRI channel 12 data need to be converted to BT data as described in Section 3.2.

The gradients in the zonal and meridional directions of the BT images are calculated separately as follows:

$$G_x(x,y) = \frac{(H(x+1,y) - H(x-1,y))}{2} \tag{10}$$

$$G_y(x,y) = \frac{(H(x,y+1) - H(x,y-1))}{2} \tag{11}$$

where $x$ and $y$ are the coordinates of the corresponding image element and $H(x,y)$ is the BT of the corresponding image element, $G_x(x,y)$ is the BT gradient in the longitude direction of the corresponding image element, and $G_y(x,y)$ is the BT gradient in the latitude direction of the corresponding image element. In comparison with the gradient calculation method proposed by Xie et al. [25], the points $x + 1, y$ and $x - 1, y$ are used to calculate the gradient with Equation (10), which means moving 2 steps in $x$ (and the same for $y$ in Equation (11)). This is performed because typhoons exhibit high BTP values not only in their central regions but also in other areas, which can have a certain impact on the localization results. Utilizing this method for gradient calculation can to some extent suppress interference from non-central regions and improve localization accuracy.

The BT gradient $G_{BT}$ of the typhoon is obtained as follows:

$$G_{BT} = \sqrt{(G_x(x,y))^2 + (G_y(x,y))^2} \tag{12}$$

The divergence of the BT gradient is used to represent the intensity magnitude of the vector field emanation at individual points in space:

$$div\ G_{BT} = \frac{\delta G_x(x,y)}{\delta x} + \frac{G_y(x,y)}{\delta y} \tag{13}$$

where $div\ G_{BT}$ is the divergence of the BT gradient. The curl of the BT gradient is used to express the degree of rotation caused by the vector field near a point of the micro-element in the region:

$$curl\ G_{BT} = \left(\frac{\delta G_y(x,y)}{\delta x} - \frac{\delta G_x(x,y)}{\delta y}\right) \cdot \vec{k} \tag{14}$$

where $curl\ G_{BT}$ is the curl of the BT gradient, and $\vec{k}$ is the curl direction. The BTP value $P$ to the typhoon cloud system is calculated using divergence and curl:

$$P = \sqrt{(div\ G_{BT})^2 + (curl\ G_{BT})^2} \tag{15}$$

Search for the BTP maximum within a 40 km radius around the geometric center of the cloud system, with a search step of 8 km. Then, using the location of this maximum as the center, search for the BTP minimum within an 8 km by 8 km area, which is identified as the typhoon center.

## 4. Results

### *4.1. Typhoon Cloud System Identification and Correction of Parallax*

The algorithm developed in this study was tested by application to FY-4A AGRI level 1 data over the study area (Section 2.1) collected for typhoon HL (Table 1), on 6 November 2019, at 02:00 Beijing time, as an example. Figure 4a shows the initial data corresponding to the study area. A map showing the spatial distribution of the BT over the study area, obtained after image pre-processing as described in Section 3, is presented in Figure 4b. Normally, the cloud top temperature is much lower than that of the sea and land surface. Thus, the BT map shows the locations of the cloud systems in the study area as dark blue areas with low CTT. To accurately extract the dark blue regions in the BT spatial distribution map, the BT data were converted to binary data by using the Fisher criteria for small and large intra-class variances to automatically find the thresholds. The result, i.e., the binary map in BT space, is presented in Figure 4c. To identify candidate typhoon cloud systems, erosion and expansion were applied and small cloud systems were removed. The results in Figure 4d show that the remaining cloud systems cover large areas and can be considered as candidate typhoon cloud systems. After calculating the center of mass of each candidate cloud system, the center of mass of the cloud system closest to the typhoon center in the previous observation (the cloud system at about 20°N, 150°E) was selected as the target typhoon cloud system. The result in Figure 5a shows that the typhoon cloud system has an overall lower CTT, while the CTT in the eye of the typhoon is substantially higher. This temperature distribution is in good agreement with the properties of a typhoon system with an eye. FY-4A cloud top height products were used for parallax correction, i.e., to match the longitude and latitude of each pixel to the surface longitude and latitude. The result after the application of the parallax correction to the data in Figure 5a is presented in Figure 5b. The results before and after parallax correction in the typhoon eye area are shown in Figure 5c,d. It can be found that the latitude and longitude of the typhoon eye area were significantly adjusted.

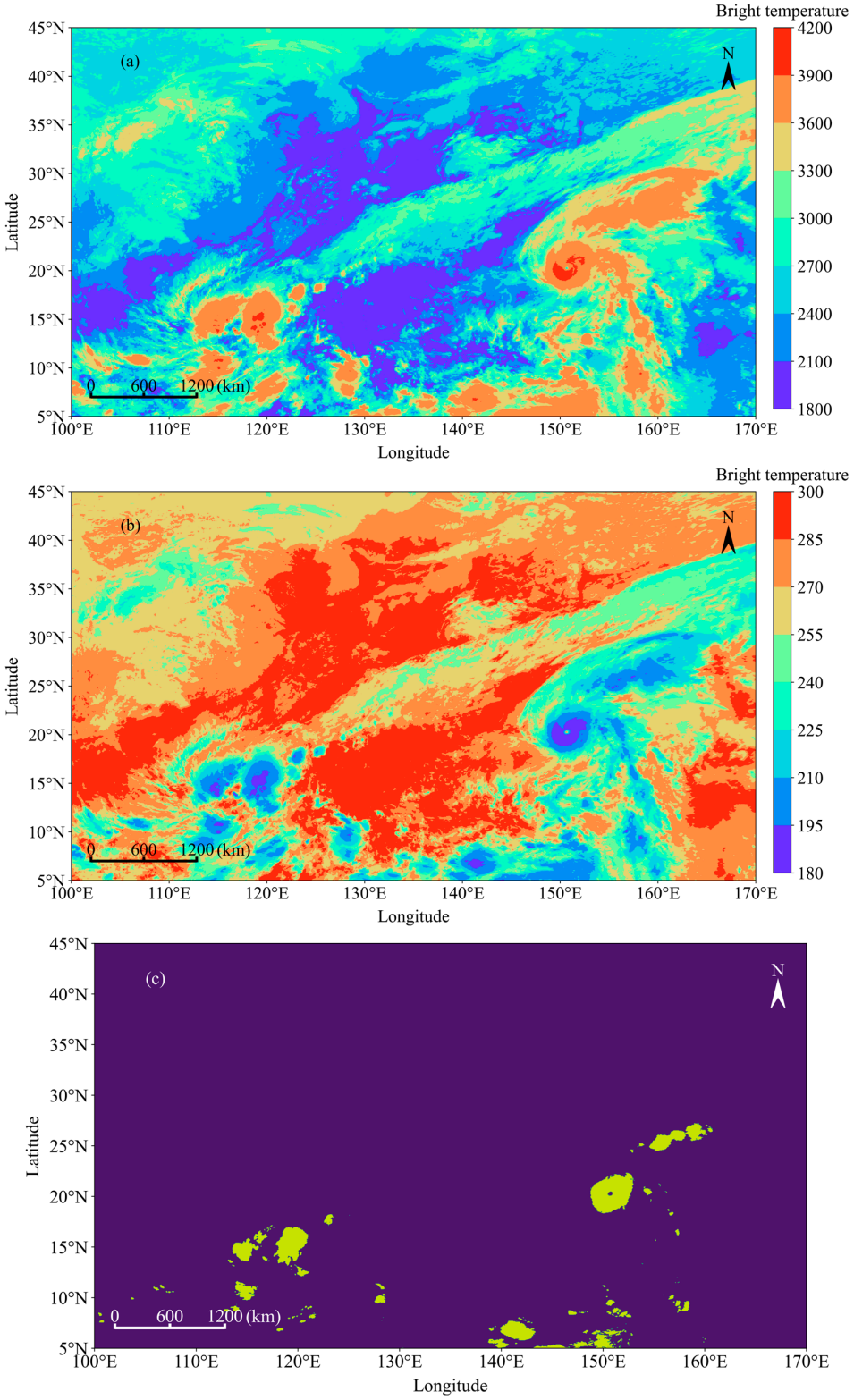



**Figure 4.** *Cont.*

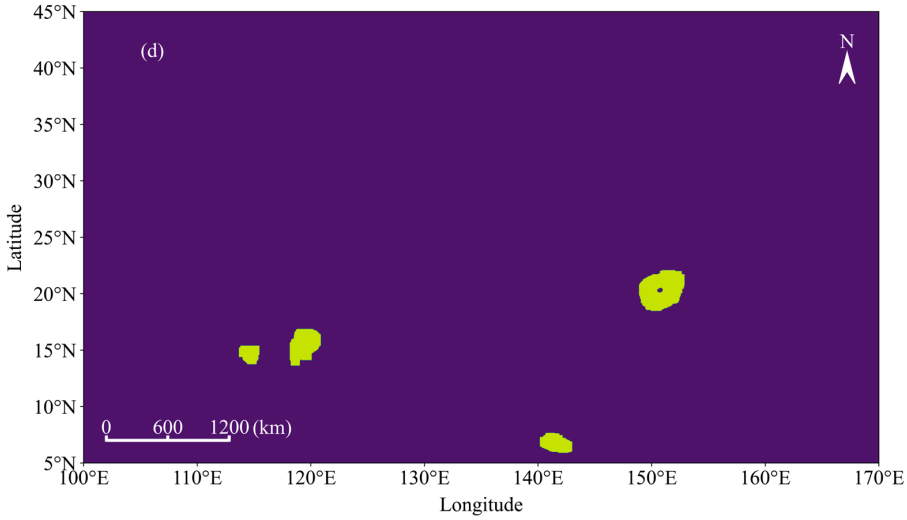



**Figure 4.** The application of the typhoon detection algorithm to identify the typhoon cloud system over the northwest Pacific using FY-4A AGRI level 1 data on 6 November 2019, at 02:00 Beijing time (typhoon HL). (**a**) The initial data after projection conversion pre-processing, (**b**) the spatial distribution of the BT over the study area (unit: K), (**c**) the binarized image of the BT spatial distribution, and (**d**) further processing that shows the locations of candidate target cloud systems.

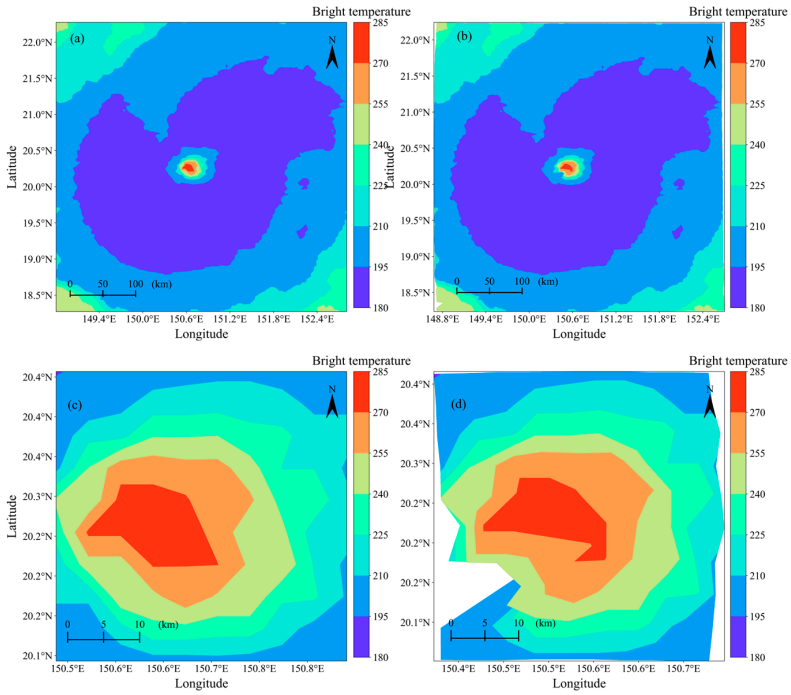



**Figure 5.** The BT distribution of the typhoon cloud system using FY-4A AGRI level 1 data on 6 November 2019, at 02:00 Beijing time: the BT distribution of the target cloud system before (**a**) and after (**b**) parallax correction. (**c**) and (**d**) show details of the typhoon eye area before and after parallax correction, respectively.

### *4.2. Results from the Brightness Temperature Perturbation Typhoon Localization Algorithm*

To accurately determine the typhoon center, the operations described in Section 3.5 were executed using the BT data presented in Figure 5b. First, the longitudinal and latitudinal BT gradients were calculated. The results in Figure 6a,b show that the typhoon eye feature is enhanced in the center of the eye and that clear BT maxima and minima occur between the typhoon cloud area and the eye area. These minima and maxima reflect

that the sea surface temperature is higher than the CTT, which can only be observed in the cloud-free typhoon eye area. Therefore, there is a large BT gradient across the junction of the typhoon eye area and the cloud area, and BT maxima and minima occur.

Using the gradients, the BT divergence and curl can be calculated and the results are presented in Figure 6c,d, respectively. Figure 6c,d show the clear structures in the BT divergence and curl in the typhoon eye. A negative BT divergence indicates convergence, which in turn indicates that the weather situation is favorable for further enhancement and development in convective weather such as cyclones. The BT curl reaches a maximum in the eye area, indicating strong convergence, and is smaller in the cloud area.

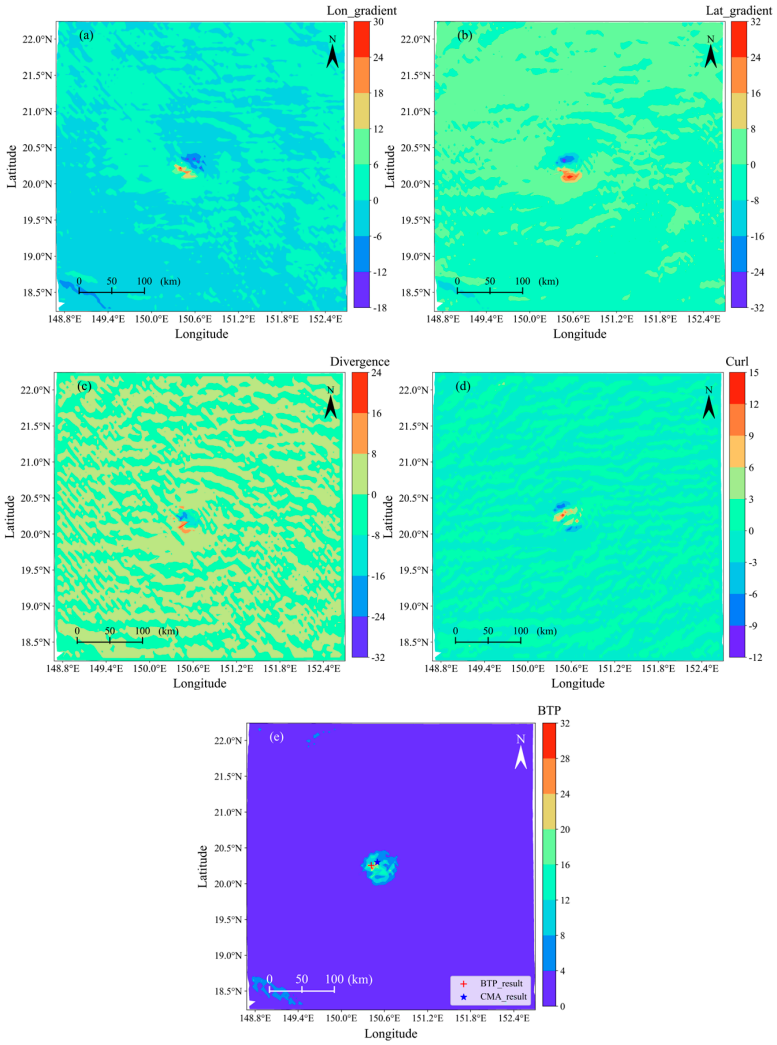



**Figure 6.** Results from the BTP typhoon localization algorithm applied to FY-4A AGRI level 1 data over the northwest Pacific on 6 November 2019, at 02:00 Beijing time (typhoon HL): (**a**) the longitudinal BT gradient near the typhoon eye area (unit: km); (**b**) latitudinal BT gradient near the typhoon eye area; (**c**) spatial distribution of BT divergence (unit: $N{\cdot}m^{-3} \times 10^7$); (**d**) spatial distribution of the BT curl (unit: $N{\cdot}m^{-3} \times 10^7$); (**e**) spatial distribution of BTP. The location of the typhoon as determined from the BTP distribution is indicated with a red + and the location of the typhoon center provided by CMA is indicated with a blue star.

Using the BT divergence and curl, the BTP can be calculated and the BTP spatial distribution over the typhoon cloud area is presented in Figure 6e. The results well describe the BTP characteristics of the typhoon center, showing that the perturbation in the eye area is substantially larger than that in the cloud area. In the cloud area, only the cloud top BT can be observed, for which the BT difference is very small and thus the BTP value is also small.

Using the BTP data, the location of the typhoon center is determined at 20.25°N, 150.42°E. This location compares favorably with that for the typhoon center provided

by CMA at 20.3°N, 150.5°E. These locations are indicated in Figure 6e and the distance between them is 9.43 km, about two pixels.

### *4.3. STC SIFT Typhoon Localization*

The typhoon localization method using STC SIFT features (see Section 3.4) is illustrated in Figure 7. Previous images are shown to the left of Figure 7a,b, and current images are shown at the right. Feature points in the current and previous images are extracted as shown in Figure 7a. The feature points in both images are matched, and filtered using the STC and rotation uniform distribution filtering algorithms. The STC filtering removes feature points with large errors in the matching results, and the rotation uniform distribution makes the feature points evenly distributed across the image, as shown in Figure 7b. The matching lines between the filtered feature points are approximately parallel to each other. The minimum distance deviation and minimum angle deviation are calculated using the filtered feature points to obtain the typhoon center location as described in Section 3.4. The results are presented in Figure 7c. The optimum typhoon center location is 20.43°N, 150.43°E. The location of the typhoon center provided by CMA is 20.3°N, 150.5°E, and the difference is 14.76 km, about three pixels.

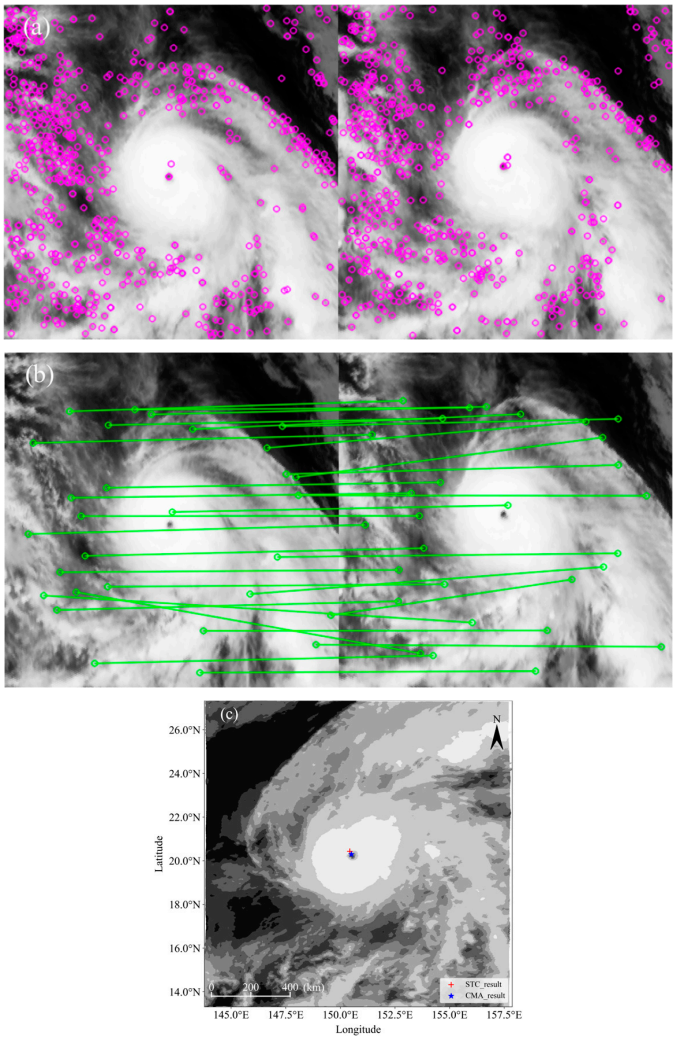



**Figure 7.** Typhoon center localization with the STC SIFT feature method using FY-4A AGRI level 1 data on 6 November 2019, at 02:00 Beijing time (typhoon HL): (**a**) feature point distributions in the extracted historical image (**left**) and the current image (**right**); (**b**) results of matching the remaining feature points after STC filtering and rotation uniform distribution filtering; (**c**) the comparison of the final positioning result (red +) with the typhoon center location provided by CMA (blue star).

## 5. Analysis

The application of two typhoon center localization methods, BTP and STC, has been illustrated by using data from typhoon HL observed by FY-4A AGRI on 6 November 2019, at 02:00 Beijing time. The results were evaluated by comparison with the best path data provided by CMA. The BTP and STC methods were also applied to six other typhoons, with characteristics listed in Table 1 and the quantity of observational data under different typhoon intensities listed in Table 2. The positioning accuracy of typhoons is related to the typhoon observation time sampling, the intensity of the typhoon itself, and the typhoon positioning method used. The average accuracies of the localization of the centers of these seven typhoons using the BTP and STC methods, for different observation time resolution periods and different typhoon intensities, are presented in Table 3 and discussed below. The optimal paths were determined by the application of the two typhoon positioning methods to four typhoons (SD, HMN, HL, and HK), which were observed with a time resolution of 1h. The comparison of the results with the best paths provided by CMA is presented in Figure 8. The data in Figure 8 show that both methods provide relatively good positioning accuracy. Additionally, Table 4 presents the typhoon localization accuracy for the blue-outlined area (before developing into typhoon intensity, TY) in Figure 8.

**Table 3.** Positioning accuracies (km) for selected typhoons during different intensity episodes and observations at different time samplings.

| Typhoon Name and Location Method | Time Sampling | TD | TS | STS | TY | ST | STY | Total Accuracy |
|---|---|---|---|---|---|---|---|---|
| CS_BTP | 6 h | 43.85 | 52.74 | 99.05 | | | | 78.38 |
| CS_STC | 6 h | 42.08 | 52.86 | 85.81 | | | | 69.89 |
| KPS_BTP | 6 h | 83.06 | 96.94 | 149.33 | 198.88 | | | 112.29 |
| KPS_STC | 6 h | 82.20 | 77.00 | 139.63 | 147.05 | | | 97.56 |
| MLK_BTP | 3 h | 42.61 | 57.97 | 60.40 | 48.75 | 47.00 | 43.46 | 53.27 |
| MLK_STC | 3 h | 58.93 | 56.08 | 68.50 | 86.57 | 60.59 | 70.64 | 66.41 |
| XL_BTP | 1 h | 34.90 | 26.08 | 20.81 | 24.30 | 17.41 | 11.57 | 23.42 |
| XL_STC | 1 h | 32.21 | 25.56 | 19.79 | 30.61 | 22.79 | 21.31 | 26.69 |
| SD_BTP | 1 h | 21.46 | 35.22 | | | | | 29.91 |
| SD_STC | 1 h | 19.36 | 30.87 | | | | | 26.43 |
| HNM_BTP | 1 h | | 26.93 | 17.71 | 25.51 | 21.02 | 12.19 | 18.74 |
| HNM_STC | 1 h | | 23.96 | 18.02 | 23.45 | 25.94 | 24.47 | 23.95 |
| HK_BTP | 1 h | 18.18 | 31.15 | 21.96 | 20.96 | 17.88 | 11.98 | 21.79 |
| HK_STC | 1 h | 16.34 | 29.43 | 24.01 | 27.79 | 29.03 | 27.82 | 25.09 |

**Table 4.** Accuracies of the two typhoon localization methods in the blue-outlined area (before developing into Typhoon intensity, TY) in Figure 8.

| Typhoon Name | BTP_Accuracy (km) | STC_Accuracy (km) |
|---|---|---|
| SD | 77.6 | 29.21 |
| HMN | 58.2 | 37.9 |
| XL | 38.44 | 33.28 |
| HK | 34.42 | 29.64 |

### *5.1. Analysis of Effect of Different Observation Time Resolutions*

The typhoon positioning accuracies at different observation time resolutions in Table 3 show that the overall accuracy of the typhoon center positioning improves with the increase in the time sampling of the typhoon observations. In the past, most of the typhoon track data provided by CMA had a time sampling of 3 h or 6 h, and for comparison of the results from the new algorithms, the same time sampling was used for the satellite images (CS, KPS, and MLK). The data in Table 3 show that the overall accuracy of typhoon positioning at an observation resolution of 3 h or 6 h is low, mainly because the time sampling is too

long to accurately observe changes in the nature and position of the typhoon. For lower observation time resolution, the error in the results becomes larger.

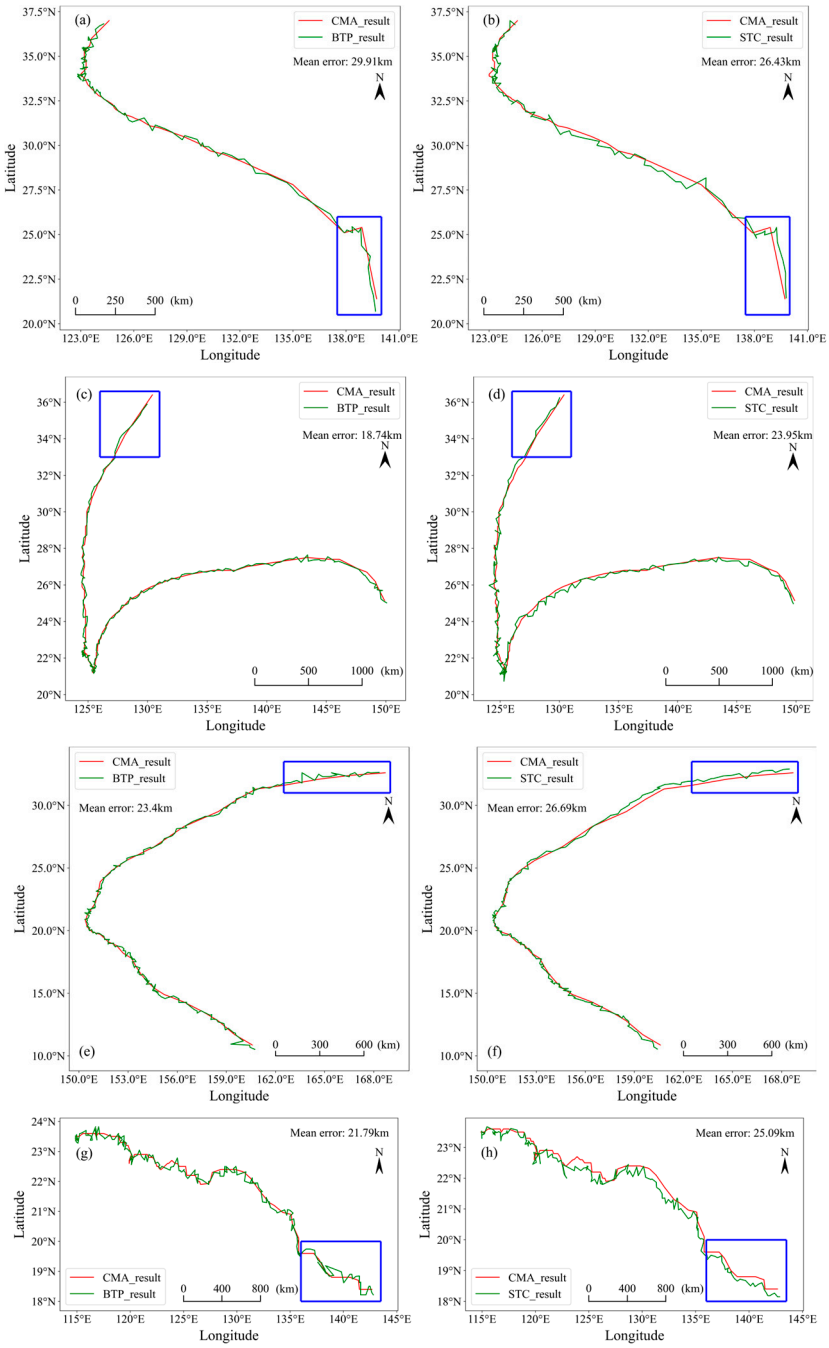



**Figure 8.** The comparison of the optimal paths of SD, HMN, HL, and HK determined using two typhoon localization methods, with the best path provided by CMA. The left column shows results from the BTP typhoon localization method and the right column shows results from the STC SIFT feature typhoon localization method for typhoons SD (**a**,**b**), HNM (**c**,**d**), HL (**e**,**f**), and HK (**g**,**h**). The average accuracy, from comparison with the CMA path, is indicated in each figure. The region outlined by blue lines delineates the portion of the typhoon characterized by lower intensity (before developing into typhoon intensity, TY). Table 4 presents the typhoon localization accuracy for the blue-outlined area.

With the development in remote sensing technology, the temporal resolution of satellite observations has been improved, and for the FY-4A satellite, it is 1h. Figure 8 shows a

comparison of the optimal paths determined using the BTP and STC methods for strong typhoons (HL, 199 validation results; HNM, 203 validation results; and HK, 187 validation results) and a weaker typhoon (SD, 115 validation results), with the best path provided by CMA, all with an observation time resolution of 1 h. For the stronger typhoon (HNM), the best result is obtained using the BTP typhoon localization method, with an average accuracy of 18.74 km (Figure 8c). For the weaker typhoon (SD), the localization using the STC SIFT method provides the best result, with an average accuracy of 26.43 km (Figure 8b). The algorithm presented in the current study has mainly been developed for observations with a time resolution of 1h, so the methods are applicable for today's observation conditions.

### *5.2. Analysis of Impact of Different Typhoon Intensities*

The positioning accuracies for typhoons of different intensities are presented in Table 3. The accuracy of the center localization results for the typhoons CS and KPS, with long time sampling (6 h), is relatively low. However, the overall typhoon positioning accuracy for CS is better than that for KPS. This is attributed to the continuous changes in the position and form of the typhoon over time, with these changes becoming more pronounced for stronger typhoons. During the three typhoon intensity stages TD, TS, and STS (see Introduction), both KPS and CS were mostly observed with a 6 h time sampling. However, the moving speed and intensity of KPS were higher than those of CS in the same stage. Consequently, in the long time sampling, the positioning accuracy decreases with the enhancement in typhoon intensity.

The time sampling of the typhoon MLK observations was 3 h, and the overall intensity of the typhoon was strong. Despite the intensification of the typhoon, there was not a significant improvement in the positioning accuracy. This is attributed to parameter settings under the 3 h time sampling, occasionally causing anomalous results due to abrupt changes in the typhoon's speed, consequently reducing the overall accuracy of the center localization of typhoon MLK. The data presented in Table 3 during the TS, STS, and TY intensity periods illustrate this scenario, with most data points indicating relatively high typhoon velocities, approximately exceeding 60 km/h. In typhoon MLK's positioning, the overall accuracy of STC SIFT typhoon localization was lower than that of BTP. During periods of lower intensity for typhoon MLK (weaker than typhoon level), the positioning accuracies for both methods were similar. However, during higher-intensity periods (typhoon level or stronger) for typhoon MLK, the accuracy of STC SIFT typhoon localization did not substantially improve while the BTP typhoon localization provided better accuracies. This decrease in accuracy during higher-intensity periods (typhoon level or stronger) for STC SIFT typhoon localization is due to the rapid changes in the typhoon's inherent characteristics during these phases. Monitored at a 3 h time sampling, the considerable variations in feature points extracted from consecutive images resulted in reduced positioning accuracy. In contrast, the BTP typhoon localization method, relying on the inherent nature of the typhoon for positioning, experienced less impact from these rapid changes.

For observations with short time sampling, such as for typhoons SD and HNM, the data in Table 3 show that the positioning accuracies are much better than those for typhoons observed in long time sampling, which confirms that the overall accuracy of the typhoon center positioning improves with the shortening of the time sampling of typhoon observation. However, the positioning accuracy of both methods does not increase together with the intensification of typhoon strength. For weaker typhoons (taking SD as an example), as the typhoon intensity increases, the positioning accuracy decreases for both methods. This is attributed to this phase being characterized by the formation or dissipation of the typhoon, where its movement speed and inherent changes accelerate with the increase in typhoon intensity, leading to decreased positioning accuracy. In the case of stronger typhoons (using HMN as an example), as the typhoon intensity increases, the accuracy of BTP typhoon localization improves, while the accuracy of STC SIFT typhoon localization does not change much. This is primarily because at a 1 h time sampling, as the typhoon intensity strengthens, the BTP typhoon localization algorithm becomes more adept

at capturing the post-change characteristics of the typhoon, while the STC SIFT typhoon localization algorithm, with this time resolution, extracts minimal changes in feature points.

### *5.3. Analysis of Impact of Different Algorithms*

The comparison of the results from the STC SIFT and BTP typhoon localization methods in Table 3 shows that, for long time sampling, the STC SIFT method provides better accuracy than the BTP method. The reason is that the STC SIFT method utilizes the whole typhoon area while the BTP method only uses the (smaller) area near the eye of the typhoon. As a result, the stability of typhoon localization with the STC SIFT is better than that of the BTP method, which is prone to missing important typhoon features when they are outside the relatively small study area or located at the edge. This phenomenon is more significant for high typhoon intensity. Taking typhoon CS as an example, the accuracy of the BTP typhoon localization method is significantly lower when the typhoon intensity is highest. Consequently, the influence of the long time sampling of 6h on the properties and localization of the typhoon is larger than that of the typhoon intensity. This leads to the conclusion that applying the BTP typhoon localization algorithm to small areas under low observation time resolution introduces significant uncertainty.

For short time sampling, the performance of the BTP typhoon localization is better than that of the STC SIFT method for typhoons with higher intensity (typhoon level or higher), and its accuracy increases with typhoon intensity, whereas the performance of typhoon localization with STC SIFT features is better for typhoons with weaker intensity (weaker than typhoon level). This is illustrated with the typhoon center localization results, using both the STC SIFT and the BTP methods, for the weaker typhoon SD, for observations with 1 h time sampling (Figure 8a,b). The localization results of the two methods for weak typhoons are quite similar. However, in Figure 8a and Table 4, the BTP typhoon localization algorithm does not perform well in the early stages of typhoon formation (the regions in the blue rectangles). Additionally, these results display significant latitude discrepancies when compared to the optimal typhoon path provided by CMA during this period. The results from the typhoon localization algorithm with the STC SIFT method in Figure 8b compare much better with the CMA path in the early stages of typhoon formation (the regions in the blue rectangles) because the STC SIFT method uses features. More feature points can be extracted as the time sampling is shorter and the movement and variation in the typhoon are smaller, which improves the localization accuracy. For the typhoons HNM (Figure 8c,d), HL (Figure 8e,f), and HK (Figure 8g,h), during their inception or dissipation stages (in the blue rectangles), the accuracy of the STC SIFT typhoon localization method consistently surpasses that of the BTP typhoon localization method, as indicated by the data in Table 4. This further substantiates the advantage of the STC SIFT typhoon localization method during periods of relatively weaker typhoons (weaker than typhoon level).

The performances of the BTP and STC SIFT methods for locating the typhoon center for a stronger typhoon are illustrated with the results from typhoon HNM, for observations with 1 h time sampling (Figure 8c,d). The results from the typhoon localization algorithm using the BTP method in Figure 8c compare very well with the optimal typhoon path of CMA. Also, the typhoon localization results using the STC SIFT method in Figure 8d show an overall satisfactory performance but with larger deviations from the CMA path than the BTP results. The high intensity of typhoon HNM, which moves fast and changes direction, results in the extraction of a smaller number of feature points and thus smaller localization accuracy. The BTP relies mainly on the spatial distribution of perturbations in the BT and the stronger the typhoon, the more significant the perturbation distribution, resulting in the better performance of the BTP method in this case. While the BTP typhoon localization algorithm demonstrates superiority in locating stronger typhoons (typhoon level or stronger), the localization results may not be accurate, as observed in the case of typhoon HK (Figure 8g) during the middle stages of typhoon development, displaying a degree of scatter. This may stem from the focus of the BTP method on the typhoon's

eye region, which may move outside the target window due to sudden increases in the typhoon's movement speed.

Furthermore, in terms of algorithm efficiency, the BTP method, targeting the typhoon's central region, is evidently more advantageous for localized studies. However, concerning algorithm stability, the STC SIFT typhoon localization, studying the entire typhoon, presents a wider research scope, reducing the likelihood of significant errors compared to BTP localization, thereby enhancing the algorithm's stability.

## 6. Discussion

This study quantified the impact of time sampling between images on the accuracy of two typhoon localization methods. Experiments were conducted using images sampled at different times, and the errors of the two typhoon localization methods with time samples of 1, 3, and 6 h were calculated with the results from the China Meteorological Administration (CMA). Since there were fewer data points for the 3 h and 6 h sampling, data from the 1 h sampling were used to supplement the calculations for these longer intervals (Table 5). For the STC SIFT method, as the time sampling increased, the median and mean errors exhibited linear growth, indicating that the longer the sampling duration, the greater the localization error. For the BTP method, the localization error also increased rapidly as the time sampling grew. When comparing the results from both methods to the CMA results, the interquartile range was smaller for the 1 h sampling, with lower uncertainty (the lower quartile error was below four pixels, and the upper quartile error was below eight pixels). However, beyond the 1 h sampling, the interquartile range for both methods increased significantly, with the lower quartile exceeding 10 pixels in the 6 h sampling.

**Table 5.** Error analysis of two typhoon positioning methods under different time samplings (unit: km).

| | Data Quantity | Mean | Median | Lower Quartile | Upper Quartile |
|---|---|---|---|---|---|
| STC_1h | 704 | 25.43 | 24.82 | 16.84 | 32.96 |
| BTP_1h | 704 | 22.69 | 19.16 | 11.23 | 28.16 |
| STC_3h | 302 | 56.41 | 52.11 | 32.07 | 70.84 |
| BTP_3h | 302 | 53.27 | 44.71 | 23.53 | 77.07 |
| STC_6h | 178 | 82.09 | 74.52 | 50.95 | 99.92 |
| BTP_6h | 178 | 93.33 | 90.99 | 63.04 | 117.2 |

The study also quantified the impact of typhoon intensity on the accuracy of the two typhoon localization methods using images with a 1 h sampling (a total of 704 typhoon data points, including 130 for TD, 138 for TS, 112 for STS, 108 for TY, 81 for ST, and 135 for STY). Experiments were conducted for typhoons of different intensities. As shown in Figure 9, the orange line inside each box represents the median error, while the green dashed line indicates the mean error. The top and bottom edges of each box denote the interquartile range, and the whiskers represent the maximum and minimum errors. For STC SIFT typhoon localization (Figure 9a), the overall accuracy did not show significant changes with increasing typhoon intensity, with the interquartile error range remaining between four and eight pixels. It is worth noting that as the typhoon intensity increased, the mean error for STC SIFT tended to be higher than the median error, indicating a greater number of higher error values with increased typhoon intensity. For BTP typhoon localization (Figure 9b), the error decreased significantly with increasing typhoon intensity. When the intensity reached or exceeded the typhoon level (TY), the interquartile range of errors was between three and six pixels. Especially at the super typhoon level (STY), the interquartile range was reduced to 2–3 pixels. Compared to BTP, STC SIFT showed an advantage in terms of fewer large errors when the typhoon intensity was below TY, providing more stable localization results. When the intensity reached or exceeded TY, BTP demonstrated significantly better localization accuracy than STC SIFT.

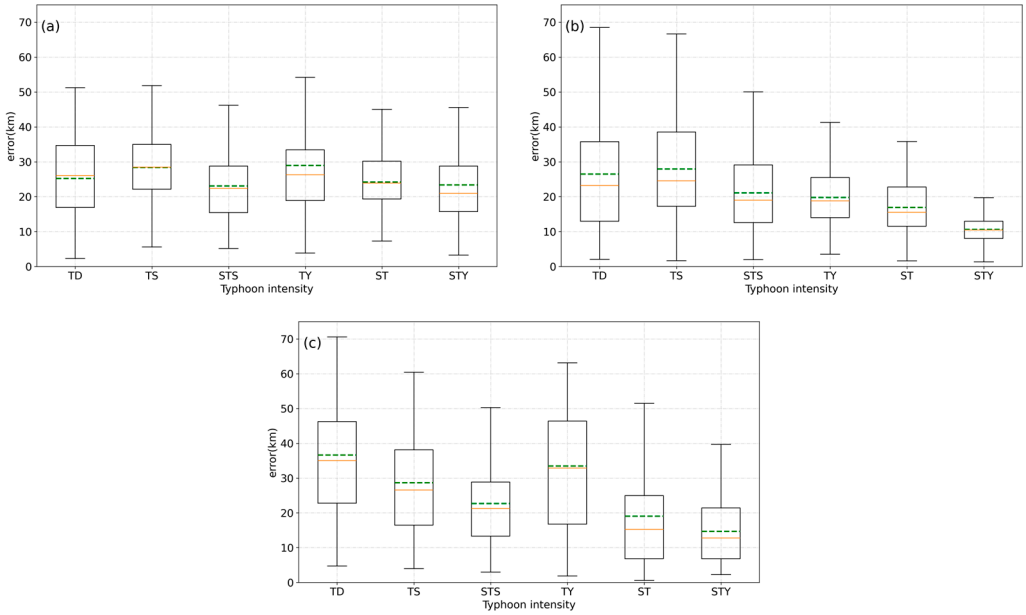



**Figure 9.** The error analysis of different typhoon localization methods under various typhoon intensities. Panel (**a**) illustrates the error analysis for STC SIFT at different typhoon intensities; panel (**b**) shows the error analysis for BTP typhoon localization under varying intensities; and panel (**c**) depicts the error analysis for BTP localization without parallax correction across different typhoon intensities. The orange line represents the median error, while the green dashed line indicates the mean error. The top and bottom edges of each box correspond to the upper and lower quartiles of the error distribution, and the whiskers denote the maximum and minimum error values.

Additionally, the study discussed the results before and after parallax correction. Figure 9c illustrates the BTP typhoon localization results without parallax correction. There was little difference between the two methods when the typhoon intensity was below TY. However, when the intensity reached or exceeded TY, the localization accuracy improved considerably. This improvement is mainly because the parallax-corrected images allowed the typhoon eye (the high-value area in BTP) to better correspond to the typhoon's best track data provided by CMA, thus enhancing localization accuracy.

In this study, two typhoon localization algorithms have been improved to achieve automated monitoring of the northwest Pacific region using the method of searching for the target cloud system and determining the geometric center of the target cloud system as the center of the intercepted image. With these improvements, the algorithms are suitable for operational applications. However, the typhoon localization accuracy of the automated search algorithm exhibits a certain degree of error in comparison to the optimal path data provided by CMA, where the overall error is mostly smaller than 20 km provided that observations are available with a 1h time resolution. However, the average error is larger than 20 km because of the influence of some extreme values. The automated algorithm proposed in this paper has slightly lower accuracy compared to that proposed by Xie et al. [25]. This is because Xie et al. [25]'s algorithm determines the center of the cropped image by referencing short-term typhoon forecast data, which performed well in experiments specific to typhoon images but lacks generality. In contrast, the automated typhoon localization in this study does not rely on short-term typhoon forecast data. It automatically identifies the initial position of the cloud system, making it applicable to most scenarios. However, instances of abrupt changes in typhoon characteristics and movement speed may lead to a certain degree of error. Nonetheless, the improved algorithm in this study enables automated monitoring of typhoons in the northwest Pacific region, better catering to operational needs, albeit with a slight reduction in localization accuracy compared to the pre-improved typhoon positioning methods.

## 7. Conclusions

In this study, two typhoon center location methods (STC SIFT and BTP) were improved and the various steps were illustrated by application to FY-4A AGRI L1 BT data and the AGRI cloud top height (CTH) product for one observation of the typhoon HL. Projection conversion, cloud system identification, and parallax correction were illustrated together with the application of the BTP and STC algorithms. Next, these algorithms were applied to the full time series for six other typhoons and the typhoon center location accuracy and the typhoon paths were compared with optimal path data provided by CMA, leading to the following conclusions.

(1) Within the time sampling range discussed in this study, as the time sampling interval shortens (with a minimum of 1 h), the localization errors of both methods compared to the results provided by CMA will significantly decrease;
(2) When typhoons are monitored with long time sampling, the STC SIFT typhoon localization method is more stable and the accuracy of the results is better than that from the BTP localization method; however, when typhoons are monitored with higher spatial resolution, the BTP localization method has an advantage over the STC SIFT typhoon localization method, especially for well-developed typhoons with high intensity (typhoon level or stronger);
(3) When a typhoon is monitored with short time sampling, the accuracy of typhoon location using the BTP method increases with the increase in typhoon intensity; in contrast, the STC SIFT typhoon localization method is more accurate during the typhoon development phase when the typhoon intensity is still weak (weaker than typhoon level) than in the developed stage with strong typhoon intensity (typhoon level or stronger);
(4) Because the BTP localization method focuses on the local typhoon eye area, while the STC SIFT typhoon localization method uses the whole typhoon, the BTP method is faster in terms of algorithm processing time, but the stability of accuracy is not as good as that of the STC SIFT typhoon localization method.

The analysis of the two typhoon center location methods shows that they both have merit, but their performances vary for different situations and different typhoon intensities when either STC or BTP provides more accurate results. The results show that automated monitoring of typhoons in the northwest Pacific can be achieved when observations are available with an observation time resolution of 1h. The methods described in this paper can serve the national meteorological industry to monitor typhoons, which is beneficial to national pre-disaster prevention work and global meteorological research. However, before operational application, the following problems need to be considered:

(1) When typhoon observations are available with a time resolution of 1h, the parameters set by each of the two methods for automated typhoon positioning are fixed. When encountering sudden changes in typhoon wind speed and shift speed, two problems may be encountered: a. the typhoon center may move outside the reduced study area where BTP localization is applied, and b. the typhoon characteristics change significantly and thus the number of available feature points extracted by the STC SIFT method decreases. Hence, these changes in typhoon wind speed and shift speed may lead to large errors in the accuracy of the center localization by both methods.
(2) The BTP localization method depends on the BT property of the typhoon. If there is no clear typhoon eye, the calculation of the location of the typhoon center can be affected by the surrounding BTP and thus reduce the positioning accuracy.
(3) The matching results of feature points may appear unevenly distributed in space and, although the use of rotation uniform distribution feature screening has a mitigating effect, it may not be sufficient to completely solve the problem.

In future research, the inclusion of parameters such as wind speed and central pressure can be considered to improve the two methods of typhoon center location.

**Author Contributions:** Conceptualization, Z.L. and C.Y.; methodology, C.Y.; software, C.Y. and J.G.; validation, C.Y. and J.G.; formal analysis, J.G.; investigation, C.Y.; resources, Z.L.; data curation, J.G. and G.d.L.; writing—original draft preparation, C.Y.; writing—review and editing, C.Y. and G.d.L.; visualization, C.Y.; supervision, J.G. and G.d.L.; project administration, Z.L.; funding acquisition, Z.C. All authors have read and agreed to the published version of the manuscript.

**Funding:** This research was funded by the Foreign Technical Cooperation and Scientific Research Program, grant no. E3KZ0301, and the National Natural Science Foundation of China, grant no. 41925019, and this paper is supported by the Li Zhengqiang Expert Workstation of Yunnan Province, grant no. 202205AF150031. The participation of Gerrit de Leeuw was supported by the Chinese Academy of Sciences President's International Fellowship Initiative, grant no. 2025PVA0014.

**Data Availability Statement:** FY4-AGRI data used in this paper were downloaded from http://satellite.nsmc.org.cn/portalsite/default.aspx (last access: 23 March 2024). Typhoon optimal path data used in this paper were made available by the China Meteorological Administration (CMA) (https://tcdata.typhoon.org.cn, last access: 23 March 2024).

**Acknowledgments:** The authors express their gratitude to the China Meteorological Administration (CMA) for providing the optimal path dataset and the National Satellite Meteorological Center for supplying FY-4A AGRI L1 and cloud top height (CTH) data.

**Conflicts of Interest:** The authors declare no conflict of interest.

## References

1. Uson, M.A.M. Natural disasters and land grabs: The politics of their intersection in the Philippines following super typhoon Haiyan. *Can. J. Dev. Stud./Rev. Can. D'études Dév.* **2017**, *38*, 414–430. [CrossRef]
2. Zhou, J.; Xiang, J.; Huang, S. Classification and Prediction of Typhoon Levels by Satellite Cloud Pictures through GC–LSTM Deep Learning Model. *Sensors* **2020**, *20*, 5132. [CrossRef] [PubMed]
3. Liu, N.; Wang, X.; Liao, M.; Fang, X. *Efficient Tropical Cyclone Center Location Based on Adaptive Image Edge Growing Approaches*; Institute of Automation, Chinese Academy of Sciences: Beijing, China, 2014; Volume 51, pp. 1493–1500.
4. Rüttgers, M.; Lee, S.; Jeon, S.; You, D. Prediction of a typhoon track using a generative adversarial network and satellite images. *Sci. Rep.* **2019**, *9*, 6057. [CrossRef] [PubMed]
5. Dvorak, V.F. Tropical Cyclone Intensity Analysis and Forecasting from Satellite Imagery. *Mon. Weather. Rev.* **1975**, *103*, 420–430. [CrossRef]
6. Olander, T.L.; Velden, C.S. The Advanced Dvorak Technique: Continued Development of an Objective Scheme to Estimate Tropical Cyclone Intensity Using Geostationary Infrared Satellite Imagery. *Weather. Forecast.* **2007**, *22*, 287–298. [CrossRef]
7. Velden, C.S.; Olander, T.L.; Zehr, R.M. Development of an Objective Scheme to Estimate Tropical Cyclone Intensity from Digital Geostationary Satellite Infrared Imagery. *Weather. Forecast.* **1998**, *13*, 172–186. [CrossRef]
8. Senn, H.V.; Hiser, H.W. On the Origin of Hurricane Spiral Rain Bands. *J. Atmos. Sci.* **1959**, *16*, 419–426. [CrossRef]
9. Griffin, J.S.; Burpee, R.W.; Marks, F.D.; Franklin, J.L. Real-Time Airborne Analysis of Aircraft Data Supporting Operational Hurricane Forecasting. *Weather. Forecast.* **1992**, *7*, 480–490. [CrossRef]
10. Wong, K.Y.; Yip, C.L.; Li, P.W. A novel algorithm for automatic tropical cyclone eye fix using Doppler radar data. *Meteorol. Appl.* **2007**, *14*, 49–59. [CrossRef]
11. Liu, H.; Wang, H.; Qi, L.; Zhang, J. Typhoon Positioning Method Using Dual-Radar Zero Radial Velocity Lines and Preliminary Test. *Trop. Cyclone Res. Rev.* **2017**, *6*, 26–33. [CrossRef]
12. Yurchak, B.S. Description of cloud-rain bands in a tropical cyclone by a hyperbolic-logarithmic spiral. *Russ. Meteorol. Hydrol.* **2007**, *32*, 8–18. [CrossRef]
13. Zhang, Q.P.; Lai, L.L.; Sun, w.c. Intelligent Location of Tropical Cyclone Center. In Proceedings of the 2005 International Conference on Machine Learning and Cybernetics, Guangzhou, China, 18–21 August 2005; pp. 423–428.
14. Wimmers, A.J.; Velden, C.S. Objectively Determining the Rotational Center of Tropical Cyclones in Passive Microwave Satellite Imagery. *J. Appl. Meteorol. Climatol.* **2010**, *49*, 2013–2034. [CrossRef]
15. Rao, B.M.; Kishtwal, C.M.; Pal, P.K.; Narayanan, M.S. ERS-1 surface wind observations over a cyclone system in the Bay of Bengal during November 1992. *Int. J. Remote Sens.* **1995**, *16*, 351–357. [CrossRef]
16. Hasler, A.F.; Palaniappan, K.; Kambhammetu, C.; Black, P.; Uhlhorn, E.; Chesters, D. High-Resolution Wind Fields within the Inner Core and Eye of a Mature Tropical Cyclone from GOES 1-min Images. *Bull. Am. Meteorol. Soc.* **1998**, *79*, 2483–2496. [CrossRef]
17. Tuttle, J.; Gall, R. A Single-Radar Technique for Estimating the Winds in Tropical Cyclones. *Bull. Am. Meteorol. Soc.* **1999**, *80*, 653–668. [CrossRef]
18. Zhang, C.; Chen, Y.; Ma, L. Multi-channel Satellite Cloud Image Fusion in the Shearlet Transform Domain and Its Influence on Typhoon Center Location. In Proceedings of the Image and Graphics: 9th International Conference, ICIG 2017, Shanghai, China, 13–15 September 2017; Revised Selected Papers, Part II 9, 2017; pp. 440–451.

19. Liu, J.; Wang, X. Typhoon center location method based on FY-2 remote sensing data. *Bull. Surv. Mapp.* **2020**, *6*, 49–52. [CrossRef]
20. Velden, C.S.; Olander, T.L. Bispectral satellite technique for delineating intense convection- Applications to tropical cyclones. In Proceedings of the Conference on Satellite Meteorology and Oceanography, 9th, Paris, France, 25–29 May 1998; pp. 458–461.
21. Liu, Z.; Qiu, H.; Wu, B.; Shen, G.G. Automatic center location of non-eyed typhoon in satellite cloud image. In Proceedings of the Image Processing: Algorithms and Systems II, Santa Clara, CA, USA, 21–23 January 2003; pp. 429–436.
22. Pao, T.-L.; Yeh, J.-H.; Liu, M.-Y.; Hsu, Y.-C. Locating the typhoon center from the IR satellite cloud images. In Proceedings of the 2006 IEEE International Conference on Systems, Man and Cybernetics, Taipei, Taiwan, 8–11 October 2006; pp. 484–488.
23. Jaiswal, N.; Kishtawal, C.M. Automatic Determination of Center of Tropical Cyclone in Satellite-Generated IR Images. *IEEE Geosci. Remote Sens. Lett.* **2011**, *8*, 460–463. [CrossRef]
24. Zhang, C.; Chen, Y.; Lu, J. Typhoon center location algorithm based on fractal feature and gradient of infrared satellite cloud image. In Proceedings of the International Symposium on Optoelectronic Technology and Application 2014: Optical Remote Sensing Technology and Applications, Beijing, China, 13–15 May 2014; pp. 84–89.
25. Xie, T.; Chen, J.; Yan, J. A New Objective Typhoon Location Algorithm Considering a Perturbation Factor Based on FY-4A Brightness Temperature Data. *J. Atmos. Ocean. Technol.* **2022**, *39*, 2023–2038. [CrossRef]
26. Permyakov, M.; Kleshcheva, T.; Potalova, E.; Holzworth, R.H. Characteristics of typhoon eyewalls according to World Wide Lightning Location Network data. *Mon. Weather. Rev.* **2019**, *147*, 4027–4043. [CrossRef]
27. Magee, A.D.; Kiem, A.S.; Chan, J.C. A new approach for location-specific seasonal outlooks of typhoon and super typhoon frequency across the Western North Pacific region. *Sci. Rep.* **2021**, *11*, 19439. [CrossRef]
28. Kang, I.; Park, J. Use of GNSS-Derived PWV for Predicting the Path of Typhoon: Case Studies of Soulik and Kongrey in 2018. *J. Surv. Eng.* **2021**, *147*, 04021018. [CrossRef]
29. Wang, E.K.; Wang, F.; Kumari, S.; Yeh, J.-H.; Chen, C.-M. Intelligent monitor for typhoon in IoT system of smart city. *J. Supercomput.* **2021**, *77*, 3024–3043. [CrossRef]
30. Zhou, G.; Fang, X.; Qian, Q.; Lv, X.; Cao, J.; Jiang, Y. Application of artificial intelligence technology in typhoon monitoring and forecasting. *Front. Earth Sci.* **2022**, *10*, 974497. [CrossRef]
31. Geng, X.; Min, J.; Yang, C.; Wang, Y.; Xu, D. Analysis of FY-4A AGRI Radiance Data Bias Characteristics and a Correction Experiment. *Chin. J. Atmos. Sci.* **2020**, *44*, 679–694.
32. Di, D.I.; Ronglian, Z.; Ruize, L.A.I. Parallax shift effect correction and analysis based on Fengyun-4A advanced imager. *Acta Meteorol. Sin.* **2022**, *80*, 632–642. [CrossRef]
33. Ying, M.; Zhang, W.; Yu, H.; Lu, X.; Feng, J.; Fan, Y.; Zhu, Y.; Chen, D. An overview of the China Meteorological Administration tropical cyclone database. *J. Atmos. Ocean. Technol.* **2014**, *31*, 287–301. [CrossRef]
34. Lu, X.; Yu, H.; Ying, M.; Zhao, B.; Zhang, S.; Lin, L.; Bai, L.; Wan, R. Western North Pacific tropical cyclone database created by the China Meteorological Administration. *Adv. Atmos. Sci.* **2021**, *38*, 690–699. [CrossRef]
35. Loog, M.; Duin, R.P.W.; Haeb-Umbach, R. Multiclass linear dimension reduction by weighted pairwise Fisher criteria. *IEEE Trans. Pattern Anal. Mach. Intell.* **2001**, *23*, 762–766. [CrossRef]
36. Lowe, D.G. Object recognition from local scale-invariant features. In Proceedings of the Seventh IEEE International Conference on Computer Vision, Kerkyra, Greece, 20–27 September 1999; Volume 1152, pp. 1150–1157.
37. Yan, K.; Sukthankar, R. PCA-SIFT: A more distinctive representation for local image descriptors. In Proceedings of the 2004 IEEE Computer Society Conference on Computer Vision and Pattern Recognition, CVPR 2004, Washington, DC, USA, 27 June–2 July 2004; p. II.
38. Bay, H.; Ess, A.; Tuytelaars, T.; Van Gool, L. Speeded-Up Robust Features (SURF). *Comput. Vis. Image Underst.* **2008**, *110*, 346–359. [CrossRef]
39. Chelton, D.; Schlax, M.; Freilich, M.; Milliff, R. Satellite Measurements Reveal Persistent Small-Scale Features in Ocean Winds. *Science* **2004**, *303*, 978–983. [CrossRef]
40. Maloney, E.D.; Chelton, D.B. An Assessment of the Sea Surface Temperature Influence on Surface Wind Stress in Numerical Weather Prediction and Climate Models. *J. Clim.* **2006**, *19*, 2743–2762. [CrossRef]
41. Minobe, S.; Kuwano-Yoshida, A.; Komori, N.; Xie, S.-P.; Small, R.J. Influence of the Gulf Stream on the troposphere. *Nature* **2008**, *452*, 206–209. [CrossRef] [PubMed]
42. Wei, Y.; Zhang, R.-H.; Wang, H. Mesoscale wind stress–SST coupling in the Kuroshio extension and its effect on the ocean. *J. Oceanogr.* **2017**, *73*, 785–798. [CrossRef]


**Disclaimer/Publisher's Note:** The statements, opinions and data contained in all publications are solely those of the individual author(s) and contributor(s) and not of MDPI and/or the editor(s). MDPI and/or the editor(s) disclaim responsibility for any injury to people or property resulting from any ideas, methods, instructions or products referred to in the content.